Access to unsaturated bicyclic lactones by overriding conventional C(sp^3)−H site selectivity

9.   DFT Calculation:

Computational Methods.

Density functional theory (DFT) calculations were performed with *Gaussian 16* rev. B.01.[1] Geometry optimizations were initially performed using the global-hybrid meta-NGA (nonseparable gradient approximation) MN15 functional[2] with the def2-SVP[3,4] Karlsruhe-family basis set and the optimized structures further refined with a mix of larger basis set consisting of triple-ζ valence def2-TZVPPD (where 'D' indicates diffuse basis functions) for Pd[5,6] atom and def2-SVP[3,4] for all other atoms (BS1). Minima and transition structures on the potential energy surface (PES) were confirmed using harmonic frequency analysis at the same level of theory, showing respectively zero and one imaginary frequency. Where appropriate for cases where visual inspection of TS imaginary frequency is not obvious, intrinsic reaction coordinate (IRC) analyses[7,8] were performed to confirm that the found TSs connect to the right reactants and products.

Single point (SP) corrections were performed using MN15 functional and def2-QZVP[3] basis set for all atoms. The SMD implicit continuum solvation model[9] was used to account for the effect of hexafluoroisopropanol (HFIP) solvent on the computed Gibbs energy profile. Since HIFP solvent is not available in the list of default/pre-defined solvents in the *Gaussian 16* software, it is herein parametrised using a set of *seven* parameters.[9] These include 1) the static dielectric constant of the solvent at 25ºC (*Eps* = 16.7);[10–12] 2) dynamic (optical) dielectric constant – the square of the refractive index value of 1.275 at 20ºC was used[13] (*EpsInf = 1.625625*); 3) hydrogen bond acidity (*HBondAcidity = 0.77*)[14] and 4) hydrogen bond basicity (*HBondBasicity = 0.10*)[14], which are Abraham's *A* and *B* values respectively; 5) the surface tension of the solvent at interface (*SurfaceTensionAtInterface = 23.23*)[15] – this value is obtained from the conversion of the surface tension of HFIP at 16.14 mN/m at 25ºC[16] to cal mol^{-1} Å^{-2} used in the SMD model by the conversion factor of 1 dyne/cm = 1 mN/m = 1.43932 cal mol^{-1} Å^{-2} as outlined in the Truhlar's Minnesota Solvent Descriptor Database[17]; 6) carbon aromaticity – the fraction of aromatic carbons (*CarbonAromaticity = 0.00*) and 7) electronegative halogenicity – the fraction of halogens (*Electronegative Halogenicity = 0.60*). These parameters were specified using the keyword "SCRF = (SMD, Solvent= Generic, Read)" in *Gaussian 16*.

Gibbs energies were evaluated at the reaction temperature of 393.15 K (120ºC), using a quasi-RRHO treatment of vibrational entropies.[18,19] Vibrational entropies of frequencies below 100

cm^{-1} were obtained according to a free rotor description, using a smooth damping function to interpolate between the two limiting descriptions. The free energies were further corrected using standard concentration of 1 mol/L, which were used in solvation calculations. Unless otherwise stated, the final SMD (dichloroethane)-MN15/def2-QZVP//MN15/BS1 Gibbs energies are used for discussion throughout. *All Gibbs energy values in the text and figures are quoted in kcal mol^{-1}.* All molecular structures and molecular orbitals were visualized using *PyMOL* software.[20]

9.1. Model reaction

For computational modelling, we have chosen the following reaction (Scheme S1) for mechanistic studies.
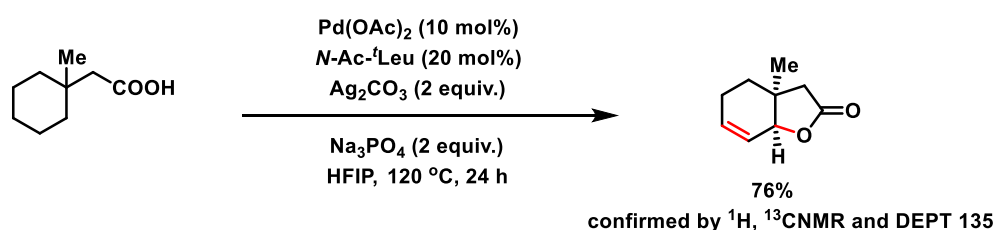
Scheme S1. Model reaction used for computational mechanistic studies.

9.2. Actual substrate for the reaction

The acid substrate in the reaction will get deprotonated by sodium phosphate, so that the actual substrate involved in the transformation will be its corresponding sodium salt. We calculated the thermodynamics for this reaction and found that the formation of sodium salt of the acid is indeed favoured, by 19.1 kcal mol^{-1} (Scheme S2).
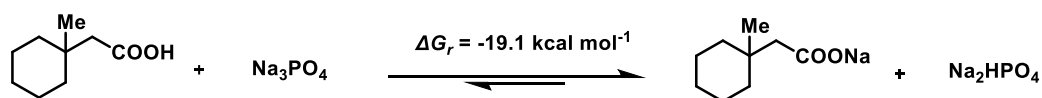
Scheme S2. Thermodynamics for the deprotonation of the acid substrate.

9.3. C–H activation transition states (TSs) – methylene vs methyl activation

The Gibbs energy profiles for the C–H activation of different H atoms are shown in Figure S2. In these transition states for the concerted metalation deprotonation (CMD) using the mono-protected amino acid (MPAA), N-acetyl *tert*-leucine, as an internal base, C–H activation can occur at either methylene carbon or methyl carbon. MPAA has been shown to lower the C–H

activation barrier over acetate ligands innate in Pd(OAc)$_2$ by forming favourable [5,6]-palladacyclic ring[21–26] conducive for C–H bond cleavage.

For the C–H activation at the methylene site, two different, prochiral H-atoms can be deprotonated, giving activated Pd–C bond either *cis* or *trans* to the methyl group. The pathway **INT1 → TS1 → INT2** *via* **TS1** forms **INT2** with Pd–C bond *cis* to the methyl group, whereas the pathway **INT1' → TS1' → INT2'** via **TS1'** forms **INT2'** with Pd–C bond *trans* to the methyl group. The pathway **INT1'' → TS1'' → INT2''** carries out C–H activation of the methyl C–H bond via **TS1''** (Figure S2).
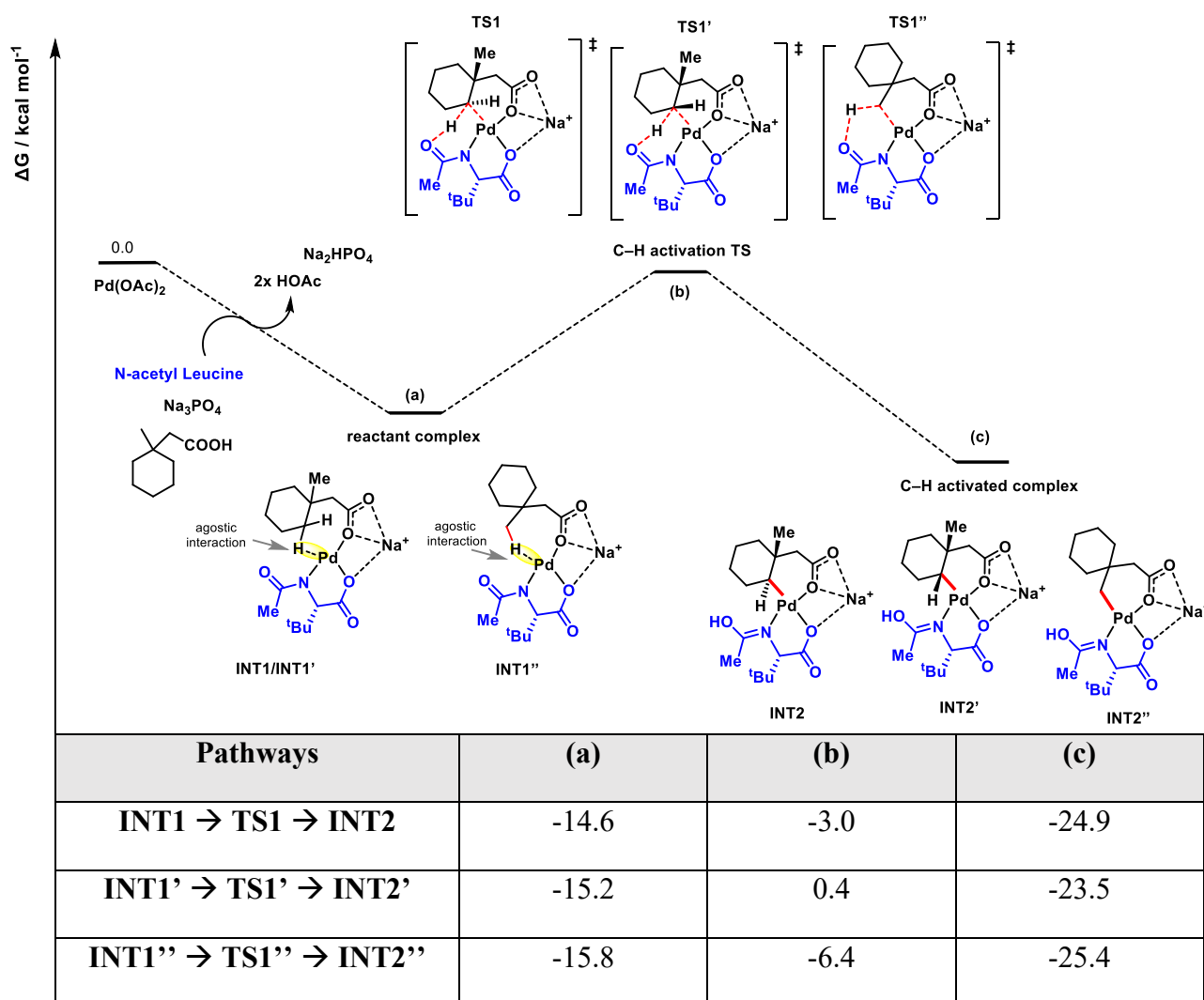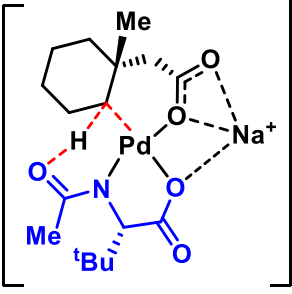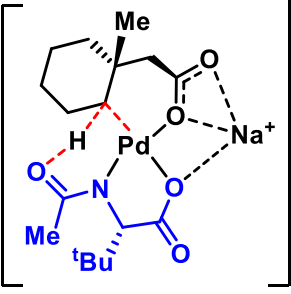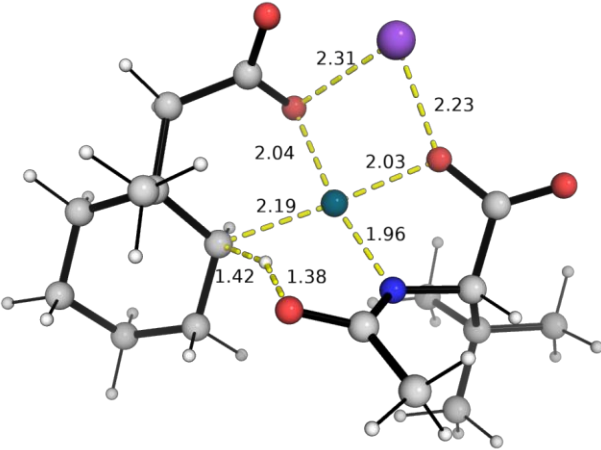

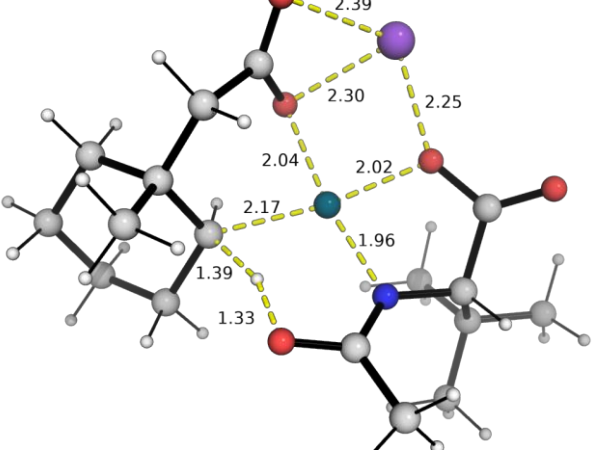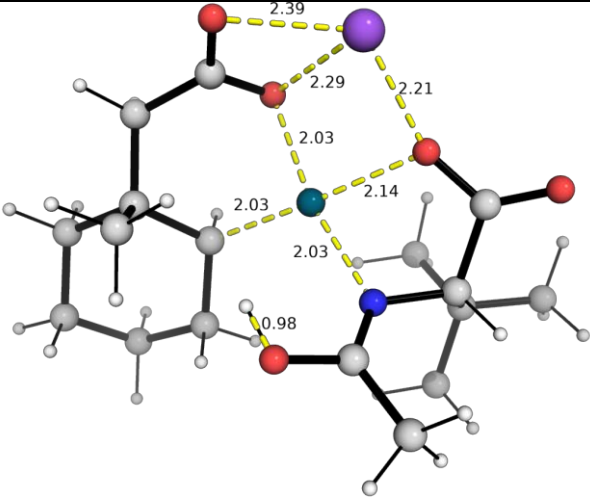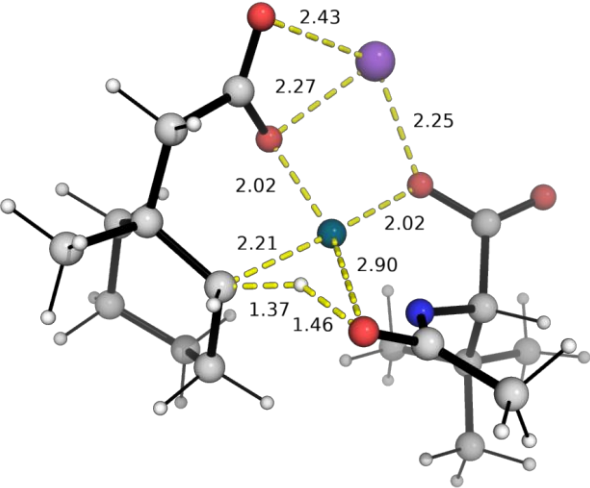| Pathways	(a)	(b)	(c)
INT1 → TS1 → INT2	-14.6	-3.0	-24.9
INT1' → TS1' → INT2'	-15.2	0.4	-23.5
INT1'' → TS1'' → INT2''	-15.8	-6.4	-25.4
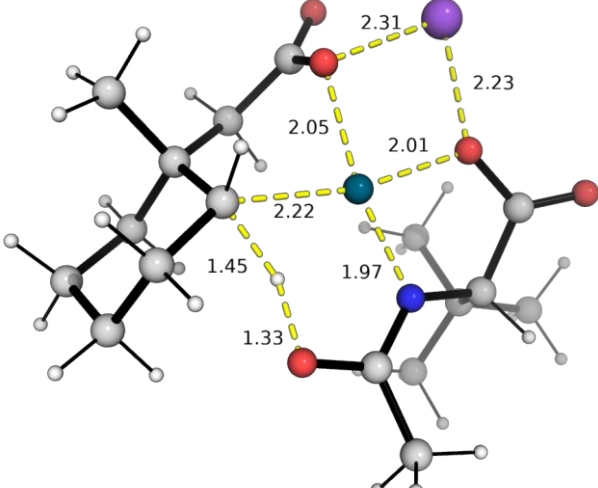
Figure S1. Gibbs energy profiles for the C–H activation step at different sites. Values are quoted in kcal mol^{-1}.

The DFT optimised structures for these TSs and their reactant and product states are shown in Figure S3. Conformational flexibility in how the acetate coordinates to the Pd-centre to form differently ring-puckered orientations (TSs with different conformations) have been considered. For methylene activation, **TS1** (at -3.0 kcal mol^{-1}) has a lower barrier than **TS1'**

(at 0.4 kcal mol⁻¹), by 3.4 kcal mol⁻¹. The activation of C(methyl)–H bond via **TS1''** has the lowest barrier, at -6.4 kcal mol⁻¹, which is lower than the C(methylene)–H activation, **TS1** by 3.4 kcal mol⁻¹. This suggests that the C(methyl)–H activation is kinetically favoured by about 78 times than C(methylene)–H at the reaction temperature of 120ºC. However, the subsequent reductive elimination of **INT2''** occurs via **TS2''** at 19.9 kcal mol⁻¹ (*vide infra*), giving a barrier of 45.3 kcal mol⁻¹ from the activated complex **INT2''**. Thus, the reductive elimination step could not occur at the reaction condition and that the C(methyl)–H activation leads to catalytic off-cycle. It is likely that **INT2''** reverts back to the reactant complex, via **TS1''**, with a backwards barrier from **INT2'' to INT1''** of 21.1 kcal mol⁻¹ than going forward with a barrier of 45.3 kcal mol⁻¹ to undergo reductive elimination.

TS1	TS1-c2
$\Delta G^{\ddagger}$ = -3.0 kcal mol⁻¹	-2.9 kcal mol⁻¹
INT2	**INT2-c2**
$\Delta G^{\ddagger}$ = -24.9 kcal mol⁻¹	

76

TS1'	TS1'-c2
$\Delta G^{\ddagger} = 0.4$ kcal mol^{-1}	2.2 kcal mol^{-1}

Structure optimises to INT2

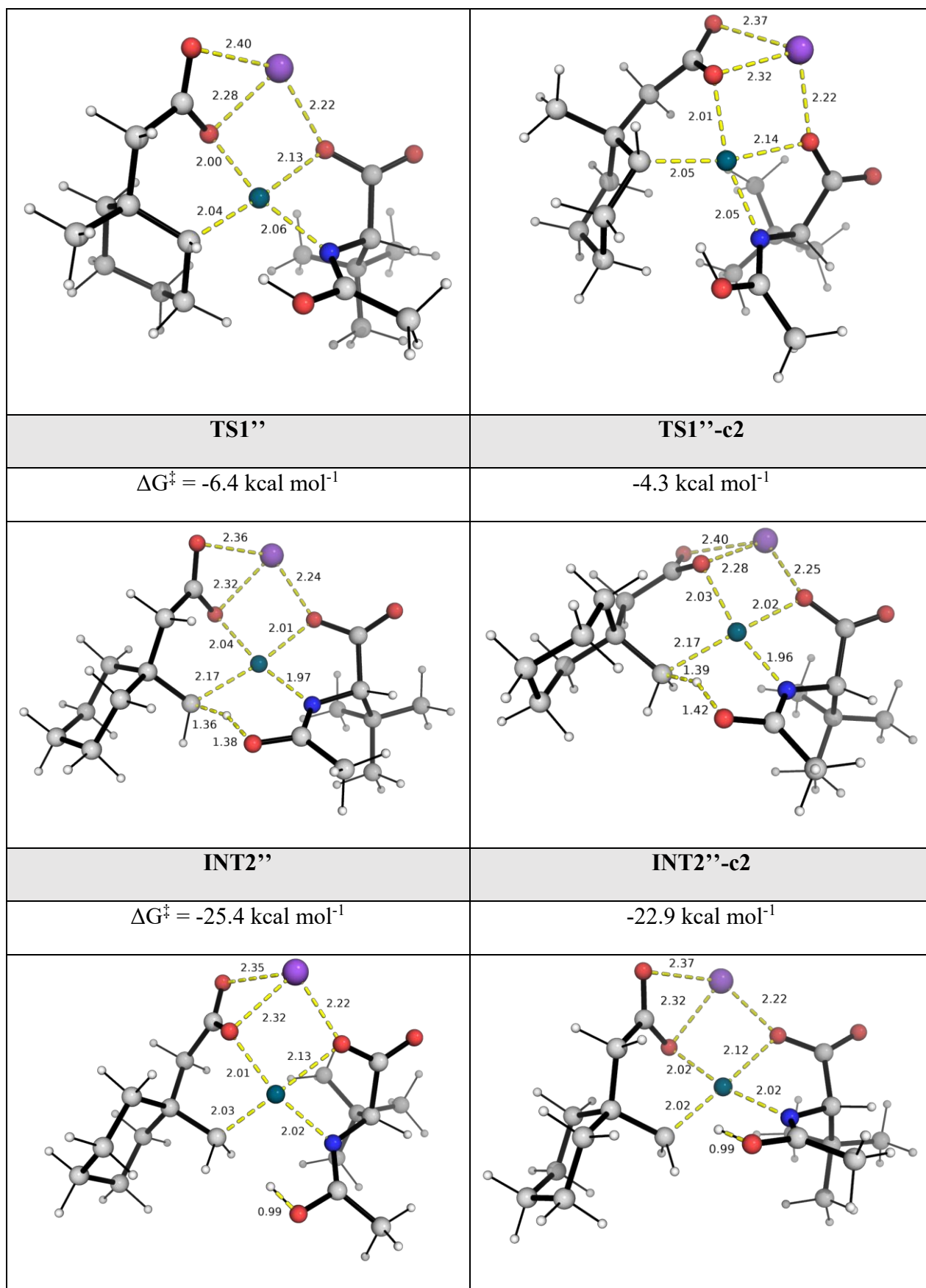| INT2'	INT2'-c2
$\Delta G^{\ddagger} = -23.5$ kcal mol^{-1}	-17.5 kcal mol^{-1}

Figure S2. DFT optimised transition state structures for the C–H activation of substrate at different sites. Activation barriers are taken relative to the sum of starting materials.

9.4. Reductive C–O bond coupling in C–H activated complexes

For the C(methyl)–H activation pathway **INT1''** → **TS1''** → **INT2''**, no β-H is available on the quaternary carbon in the C–H activated intermediate **INT2''** for elimination. We considered the alternative C–O bond formation following reductive elimination in **INT2''** to give the spirocyclic lactone product (Scheme S3a)). For the C(methylene)–H activation pathway **INT1** → **TS1** → **INT2**, in addition to β-H elimination that was considered, we also considered the alternative pathway of C–O reductive coupling to give the bicyclic lactone side product (Scheme S3b)).
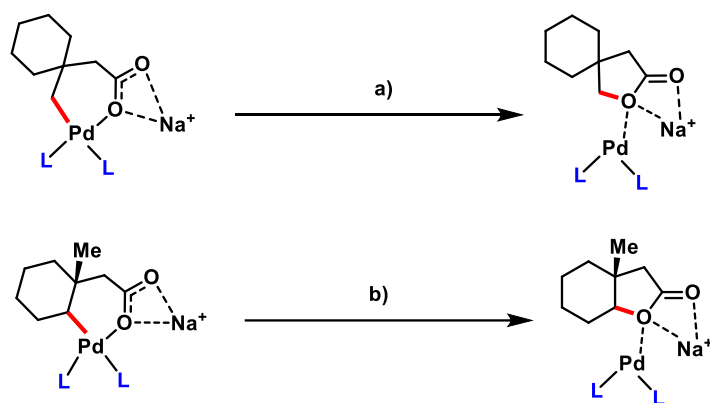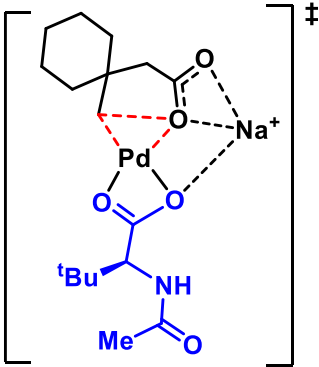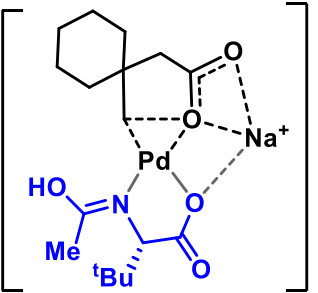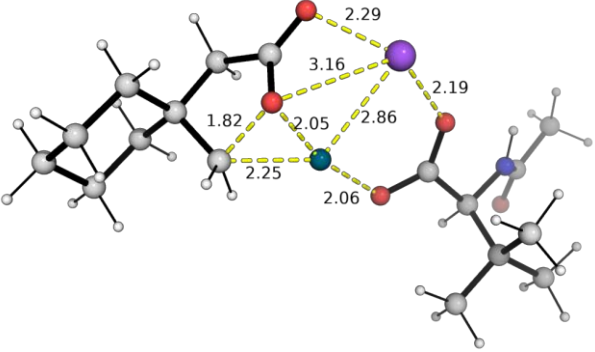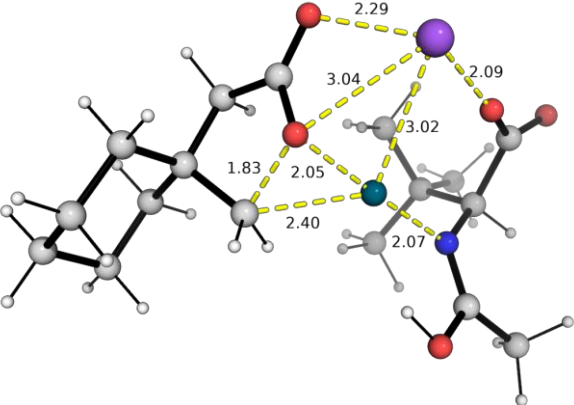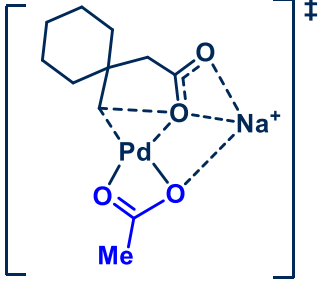

Scheme S3. Reductive C–O bond formation in a) C(methyl)–H activated complex and b) C(methylene)–H activated complex.

The optimized DFT TS structures with different ligands and conformations are shown in Figure S4 and the Gibbs energy profile for the reaction pathway following from C(methyl)–H activation is shown in Figure S5. We see that the reductive elimination with MPAA ligand coordinating in its imidic acid form (**TS2''-c2**, at 28.0 kcal mol^{-1}) has a much higher barrier than with MPAA coordinating via bidentate acetate moiety (**TS2''**, at 19.9 kcal mol^{-1}). We further note that the replacement of MPAA in **TS2''** by acetate ligand gives the C–O reductive coupling transition structure **TS2''-ac** at 19.4 kcal mol^{-1}, which is very similar to **TS2''**. This is likely because both MPAA and acetate ligands, in **TS2''** and **TS2''-ac** respectively, coordinate in a bidentate fashion (Figure S4), where both species have two Pd–O interactions; the Pd–O interactions are similar in both cases and are dominant over possible non-covalent interactions (NCIs) in the side chains of the MPAA ligand in **TS2''**.

From the Gibbs energy profile in Figure S5, we see that the activation barriers for the reductive C–O coupling is 44.8 kcal mol^{-1} (from **INT2''** to **TS2''-ac**) and 45.3 kcal mol^{-1} (from **INT2''** to **TS2''**), which are thermodynamically inaccessible at the reaction temperature of 120°C. On the other hand, the reaction from **INT2''** back to **INT1''** though **TS1''** has a barrier of 19.0

kcal mol^{-1}, which is much lower than the forward reaction from **INT2''** to **INT4''**. Thus, the C(methyl)–H activation step is reversible.

TS2''	TS2''-c2
$\Delta G^{\ddagger} = 19.9$ kcal mol^{-1}	28.0 kcal mol^{-1}
TS2''-ac	
$\Delta G^{\ddagger} = 19.4$ kcal mol^{-1}	

Figure S4. DFT optimised transition state structures for the reductive elimination to form C–O bond from the C(methyl)–H activated intermediate. Activation barriers are taken relative to the sum of starting materials.
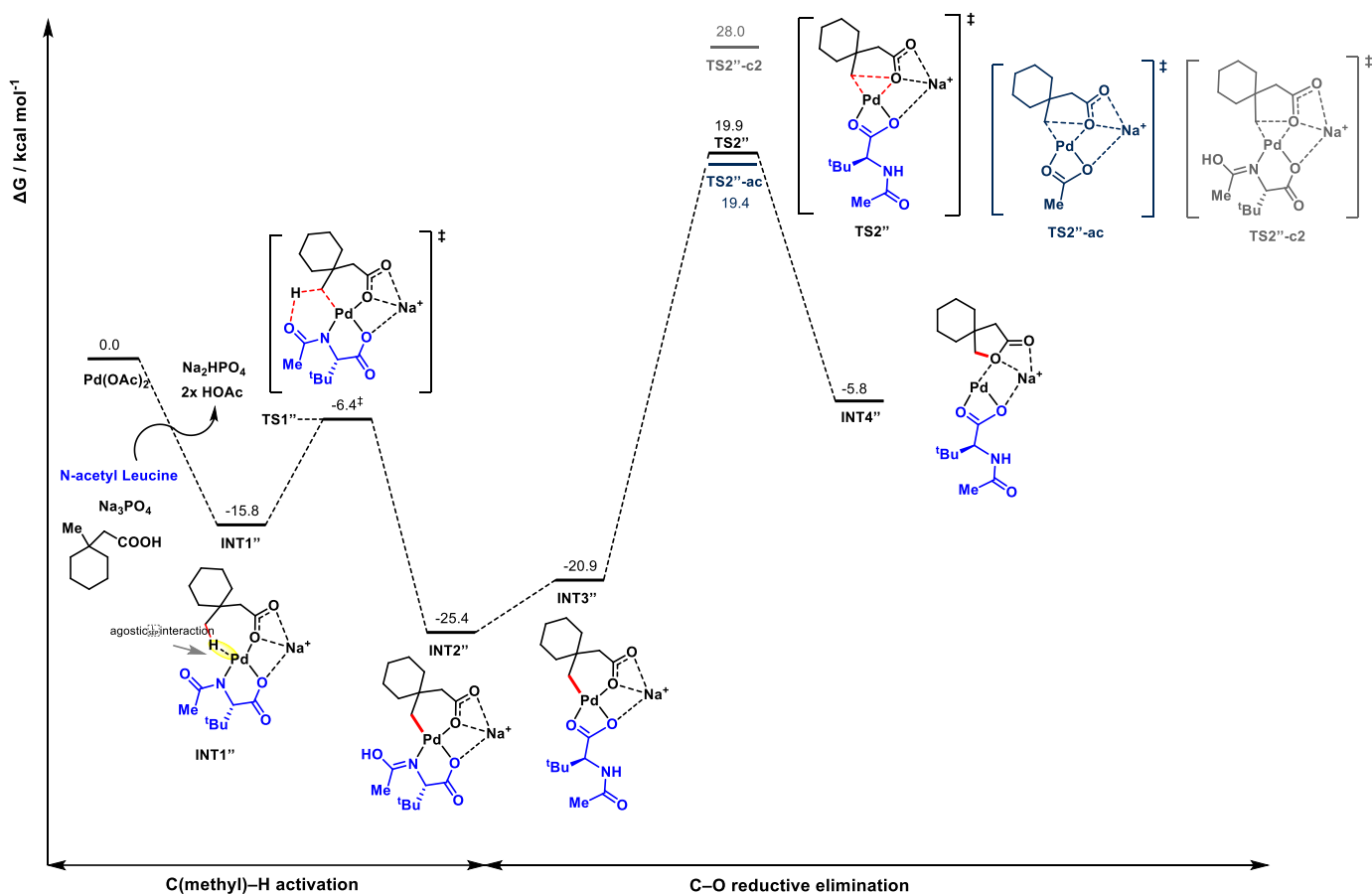
Figure S5. Gibbs energy profile for the reaction pathway following from C(methyl)–H activation.

To consider the C–O reductive coupling in the C(methylene)–H activated complex **INT2**, to give the bicyclic lactone side product (Scheme S3b)), we separately performed relaxed PES scans along the prospective C–O bond starting from optimised structure **INT2** and **INT3**. Using the highest energy structures on these PESs as initial guess, we successfully located the TSs for the C–O reductive elimination. The DFT optimised TS structures are shown in Figure S6 and the Gibbs energy profile for the reaction pathways following from C(methylene)–H

activation, comparing β-H elimination vs C–O reductive elimination, is shown in Figure S7. We note that the barriers for the C–O reductive elimination are similar to those identified C(methyl)–H activation pathway (**TS2''**, **TS2''-c2**, and **TS2''-ac**, Figure S4). In addition, these barriers (**TS3a** and **TS3b**) are much higher than the barrier for β-H elimination (**TS3**), by more than 35 kcal mol^{-1}, suggesting C–O reductive elimination is much energetically less favourable than β-H elimination.

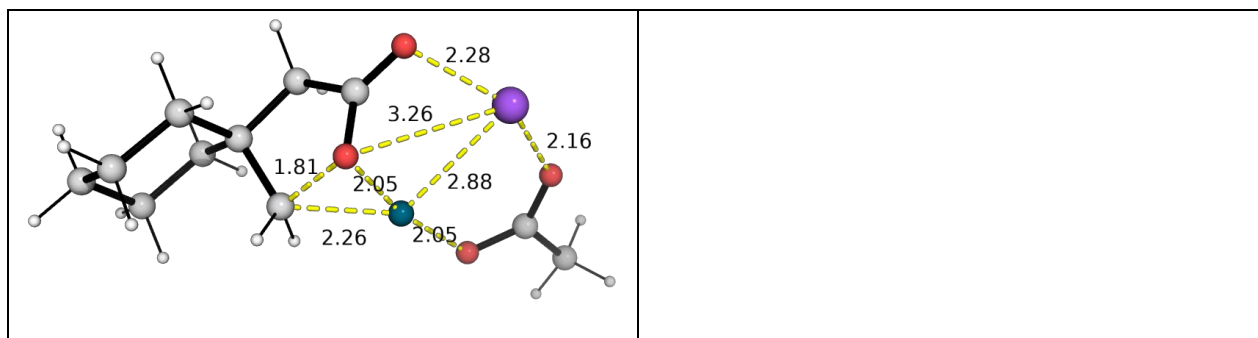| TS3a	TS3b
$\Delta G^{\ddagger} = 20.9$ kcal mol^{-1}	28.6 kcal mol^{-1}
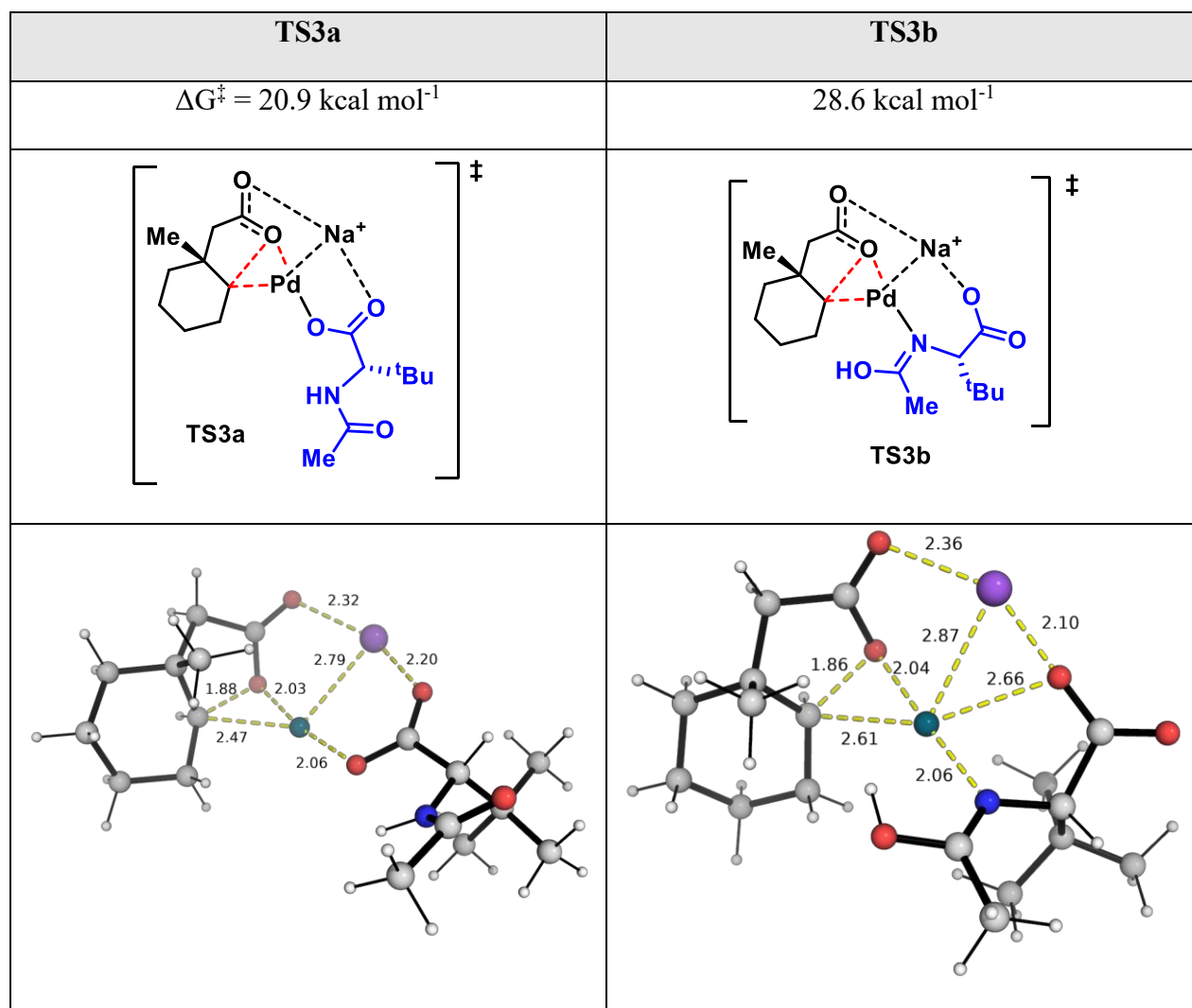
Figure S6. DFT optimised transition state structures for the reductive elimination to form C–O bond from the C(methylene)–H activated intermediate **INT2** and **INT3**. Activation barriers are taken relative to the sum of starting materials.
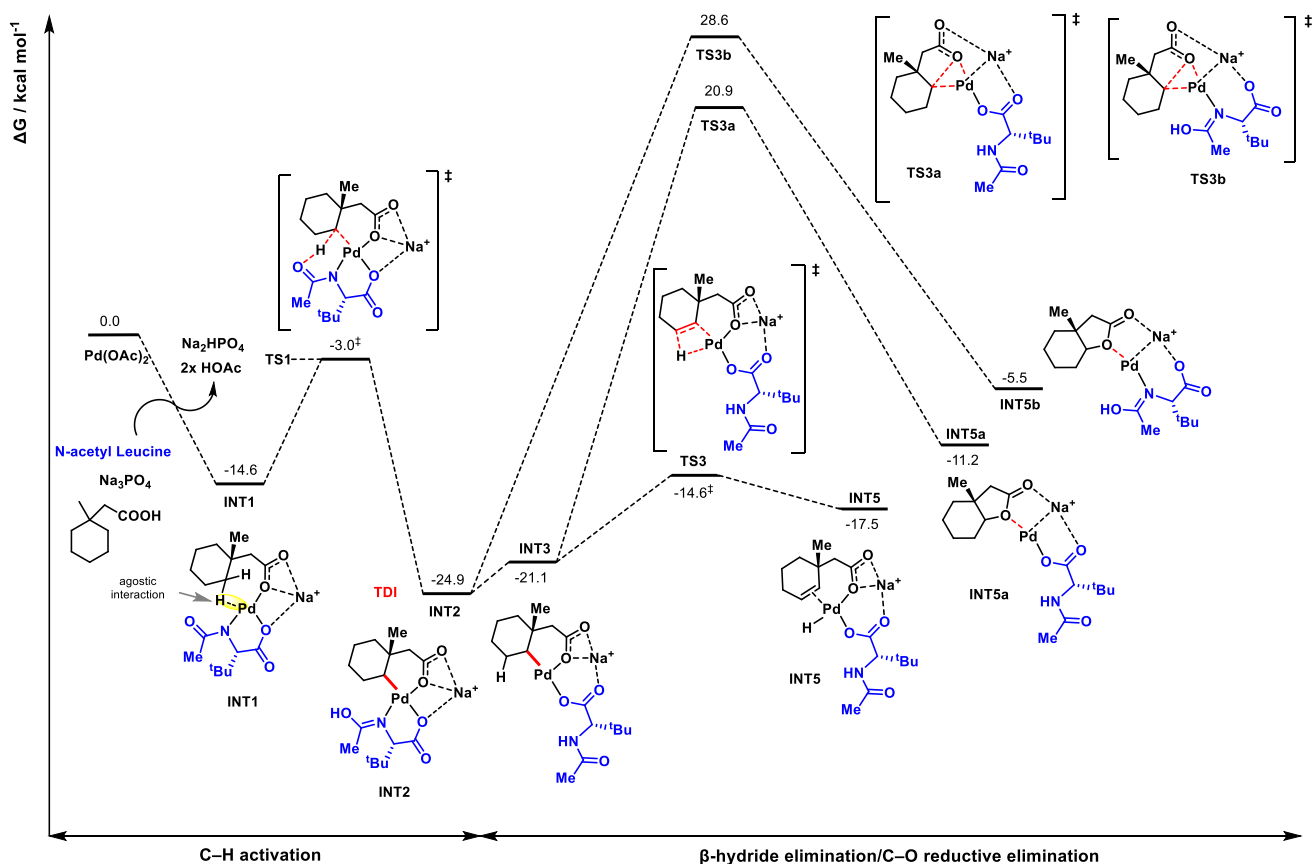
Figure S7. Gibbs energy profile for the reaction pathways (β-H elimination vs C–O reductive elimination) following from C(methylene)–H activation.

9.5. Rotational transition state for coordinating β-H to vacant Pd-site for elimination

From the C(methylene)–H activated **INT2**, a stable intermediate resulting from both **TS1** and **TS1-c2** (Figure S3), we found that the structure undergoes a rotation along the H(1)–C–C–Pd dihedral angle (**TS2**) to position one of the adjacent methylene H atoms to coordinate to the Pd-centre via agostic interaction. The DFT optimised structure **TS2** and the resulting intermediate **INT4** are shown in Figure S8.

TS2	INT4
$\Delta G^{\ddagger}$ = -16.8 kcal mol^{-1}	-18.8 kcal mol^{-1}
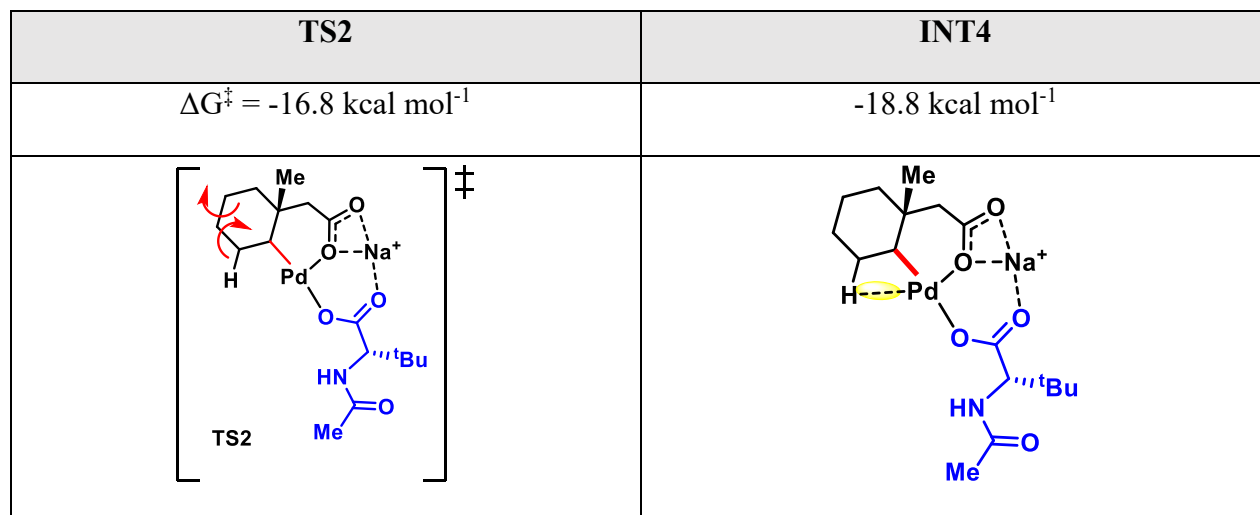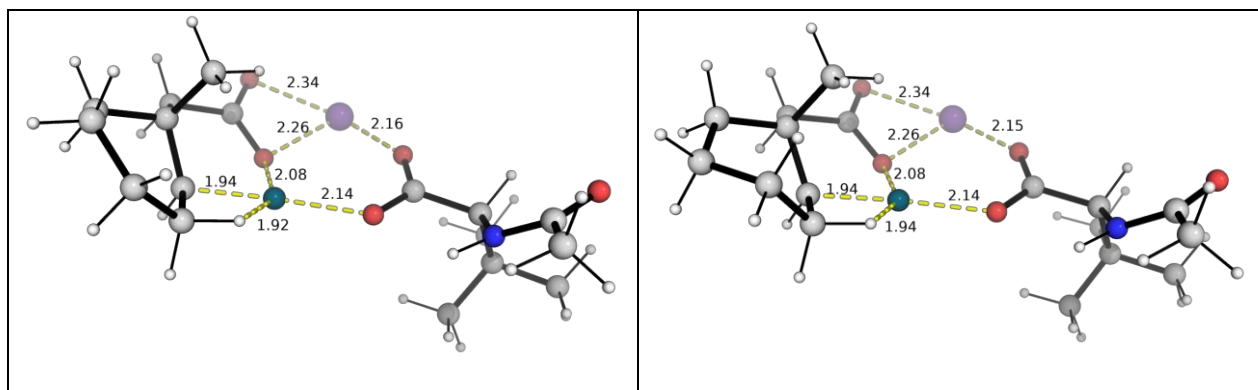
Figure S8. DFT optimised structures for the dihedral angle rotation in intermediate **INT2** to give **INT4** with CH–Pd agostic interaction. Activation barriers are taken relative to the sum of starting materials.

We note that, however, there is no such a rotational barrier to position the other H atom to coordinate to the Pd centre, as shown by the relaxed PES scan along the H(2)–C–C–Pd dihedral angle which shows no maximum point as the dihedral angle sweeps from negative value to positive value (Figure S9). This indicates that may not be a rotational barrier to bring the H(2) atom to coordinate to Pd-centre to give CH–Pd agostic interaction.
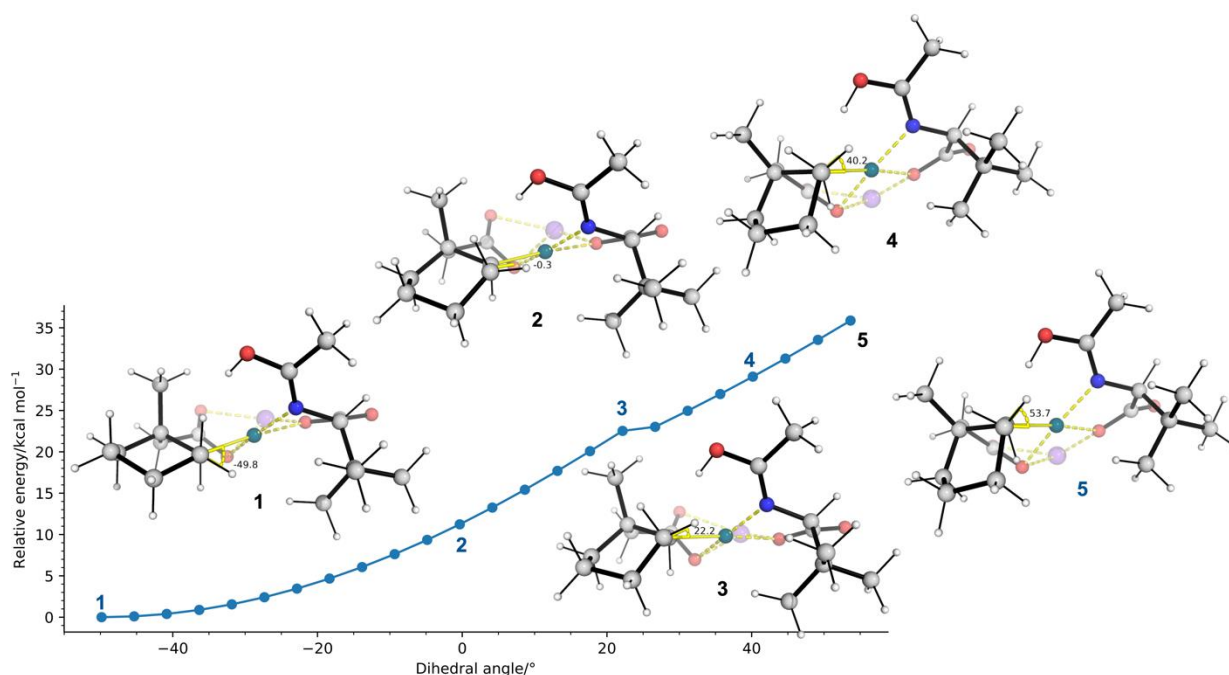
Figure S9. Relaxed PES scan in the gas-phase along H(2)–C–C–Pd dihedral angle. Gas-phase energies are used without further corrections.

9.6. Stereo determining migratory insertion TSs

Figure S10 shows the DFT optimised TS structures for the migratory insertion of the cyclohexene olefin C=C double bond into the Pd–O bond. This step is stereodetermining as the formation of new C–O bond resulting from the attack of O-atom from either side of the C=C

bond generates different stereochemistry at the fused carbons. The reaction pathway proceeding via transition state **TS4**, at 3.8 kcal mol^{-1}, gives the product with observed stereochemistry at the fused ring (*cis*-isomer). On the other hand, the reaction pathway proceeding via transition state **TS4'**, at 12.6 kcal mol^{-1}, would give the *trans*-isomer. The barrier difference of 8.8 kcal mol^{-1} suggests that **TS4** will be favoured kinetically by around 78,000 times, indicating that the *cis*-isomer will be formed predominantly, consistent with experimental observation of stereochemistry of the lactone product at the fused rings.

TS4	TS4'
$\Delta G^{\ddagger} = 3.8$ kcal mol^{-1}	12.6 kcal mol^{-1}

Figure S10. DFT optimised transition state structures for the stereodetermining migratory insertion step. Activation barriers are taken relative to the sum of starting materials.

9.7. β-H elimination TSs

β-H elimination occurs firstly after the C–H activation step to give the cyclohexene and secondly after the migratory insertion of cyclohexene C=C bond into Pd–O bond to regenerate the cyclohexene C=C bond, as the lactone ring closes. The DFT optimised TS structures for these steps are given in Figure S11.

TS3	TS5
$\Delta G^{\ddagger} = -14.6$ kcal mol^{-1}	7.5 kcal mol^{-1}

TS5-c2	**TS5-c3**
$\Delta G^{\ddagger} = 12.6$ kcal mol^{-1}	22.2 kcal mol^{-1}

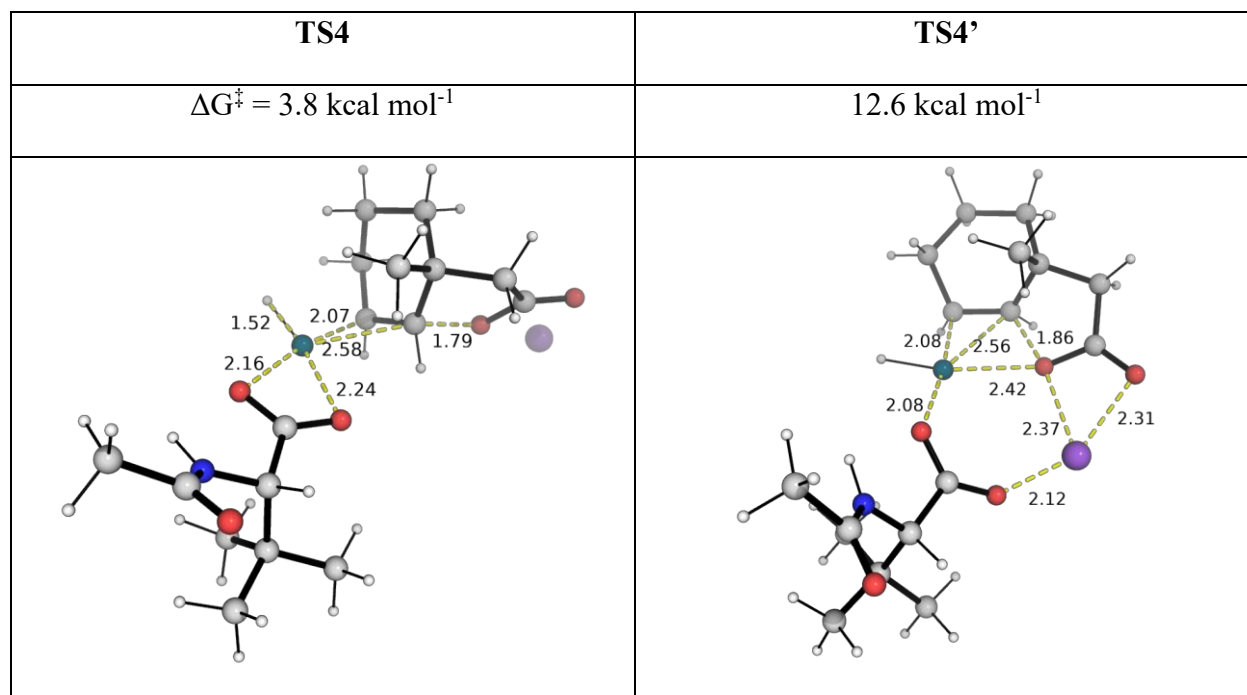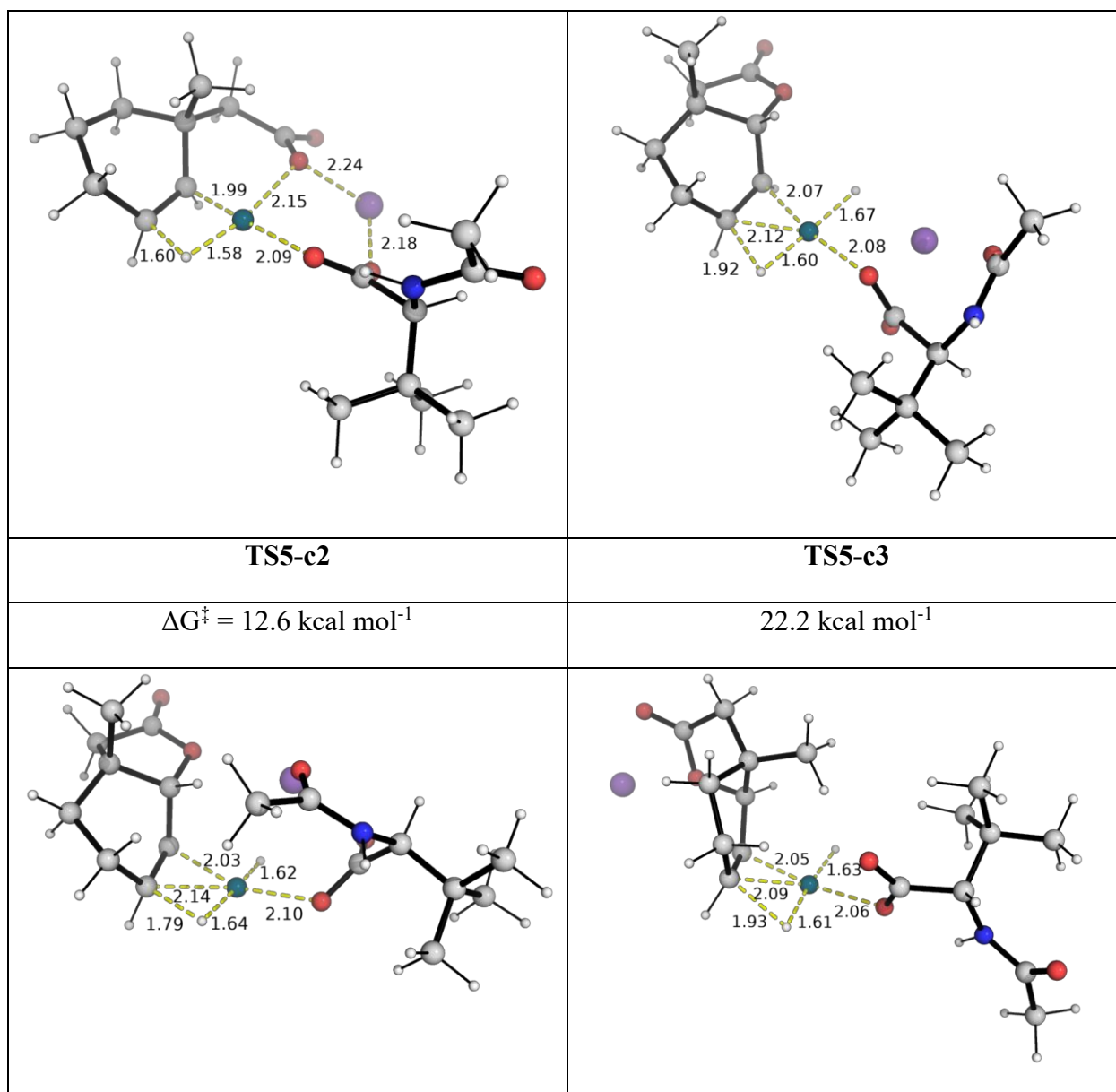**Figure S11.** DFT optimised transition state structures for the β-H elimination step. Activation barriers are taken relative to the sum of starting materials. Conformers are denoted c2, c3 etc.

9.8. Product release

The formation of palladium-bound lactone product, **INT9**, is endergonic and uphill by 6.9 kcal mol^{-1} and is thus thermodynamically disfavoured. We investigated the release of the lactone product from the catalyst centre (Figure S12).

The release of the lactone product from **INT9** in the absence of another species gives **INT10'**, with Pd centre having a vacant site (Figure S12a). This process is uphill by 16.7 kcal mol^{-1} and is unfavourable. When one HFIP solvent molecule is used to displace the product from **INT9** (Figure 12b), the resulting Pd-species formed, **INT11'**, is uphill by 14.1 kcal mol^{-1}. This is still thermodynamically unfavourable. When the silver carbonate salt is used to displace the lactone

product (Figure S12c), the resulting Pd–Ag species is thermodynamically downhill ad is thus favourable.
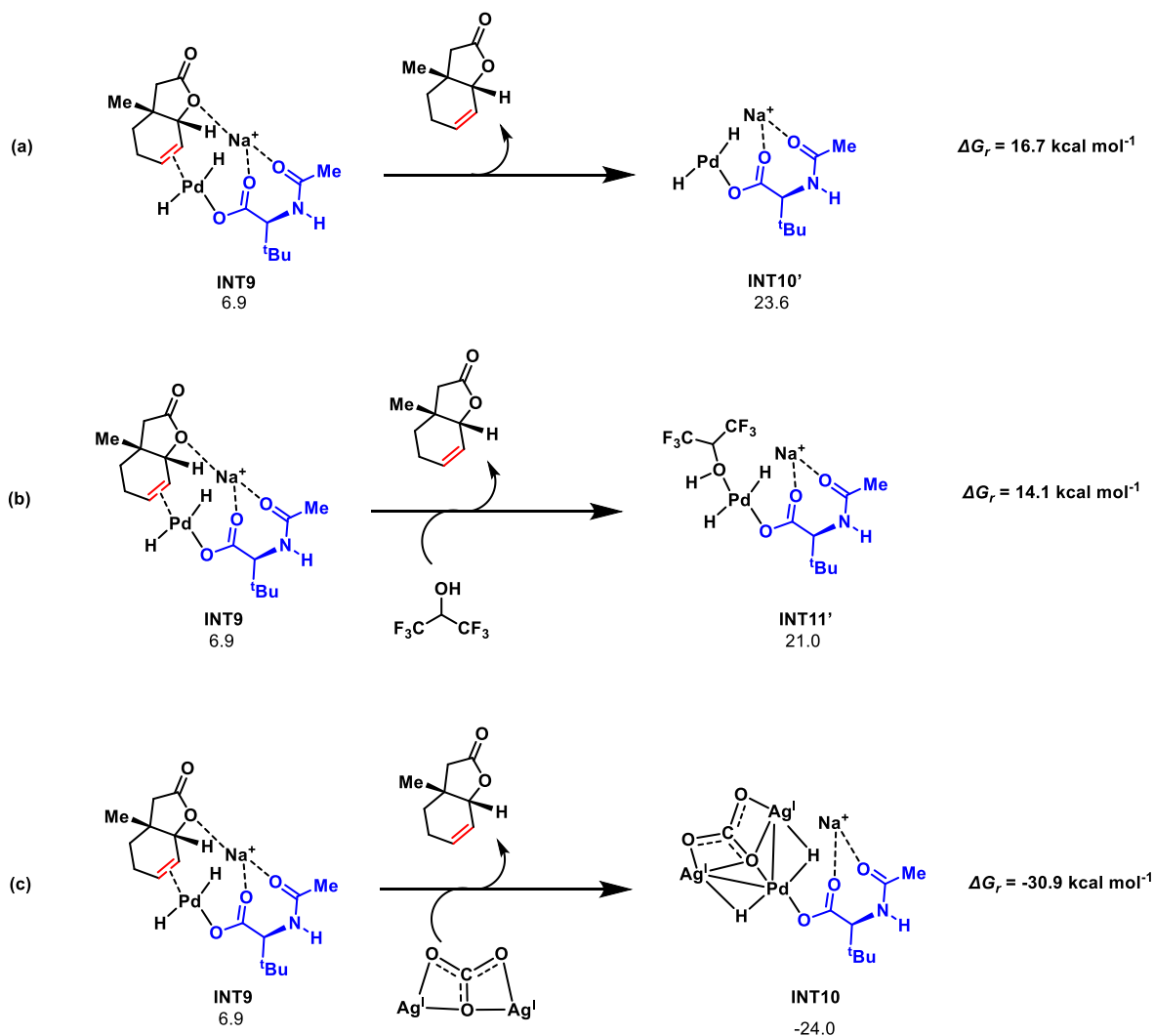
Figure S12. Thermodynamics for the release of bicyclic lactone product from Pd-catalyst.

9.9. Regioselectivity studies for 3-substituted substrate

3-Phenyl substituted substrate, where Ph and Me groups are syn to each other (relative stereochemistry), was used as a representative to study the regioselectivity outcomes for 3-substituted substrates using DFT. Herein, only a single enantiomer was used for DFT calculations as minor images of all structures are isoenergetic (the syn relation between Me and Aryl has been established through NOESY experiment). As the reaction outcomes depend on the turnover frequency-determining intermediate (TDI) and transition state (TDTS)[27], we study the energetics for these two states for the competing pathways. Figure S13 shows the associated Gibbs energy profile. Different conformations where the Me and Ph groups can be either axial or equatorial, were considered for both the TDI and the TDTS (lowest energy

conformers **INT2** and **TS5** from the study of unsubstituted substrate were used as guess structures) and the DFT-optimised structures were shown in Figure S14. For the competing pathways for the formation of regioisomeric products shown in Figure S13, the overall TDI for the reaction is **INT2Ph-equatorial,** as the C–H activation step leading to the activated complex **INT2-regio-equatorial** is reversible, such that **INT2-regio-equatorial** will revert back to the starting materials and form **INT2Ph-equatorial**, which is more thermodynamically stable (competing pathways with shared states need to take the lowest/most stable state into account)[27]. As such, the selectivity outcomes for the formation of the major vs minor product depends on the difference in the activation barriers for the TDTSs. **TS5Ph-equatorial** (at 4.3 kcal mol^{-1}) leading to the major product has a barrier that is 3.9 kcal mol^{-1} lower than **TS5Ph-regio** (at 8.2 kcal mol^{-1}) leading to the minor product. This predicts the right major product which was experimentally observed.
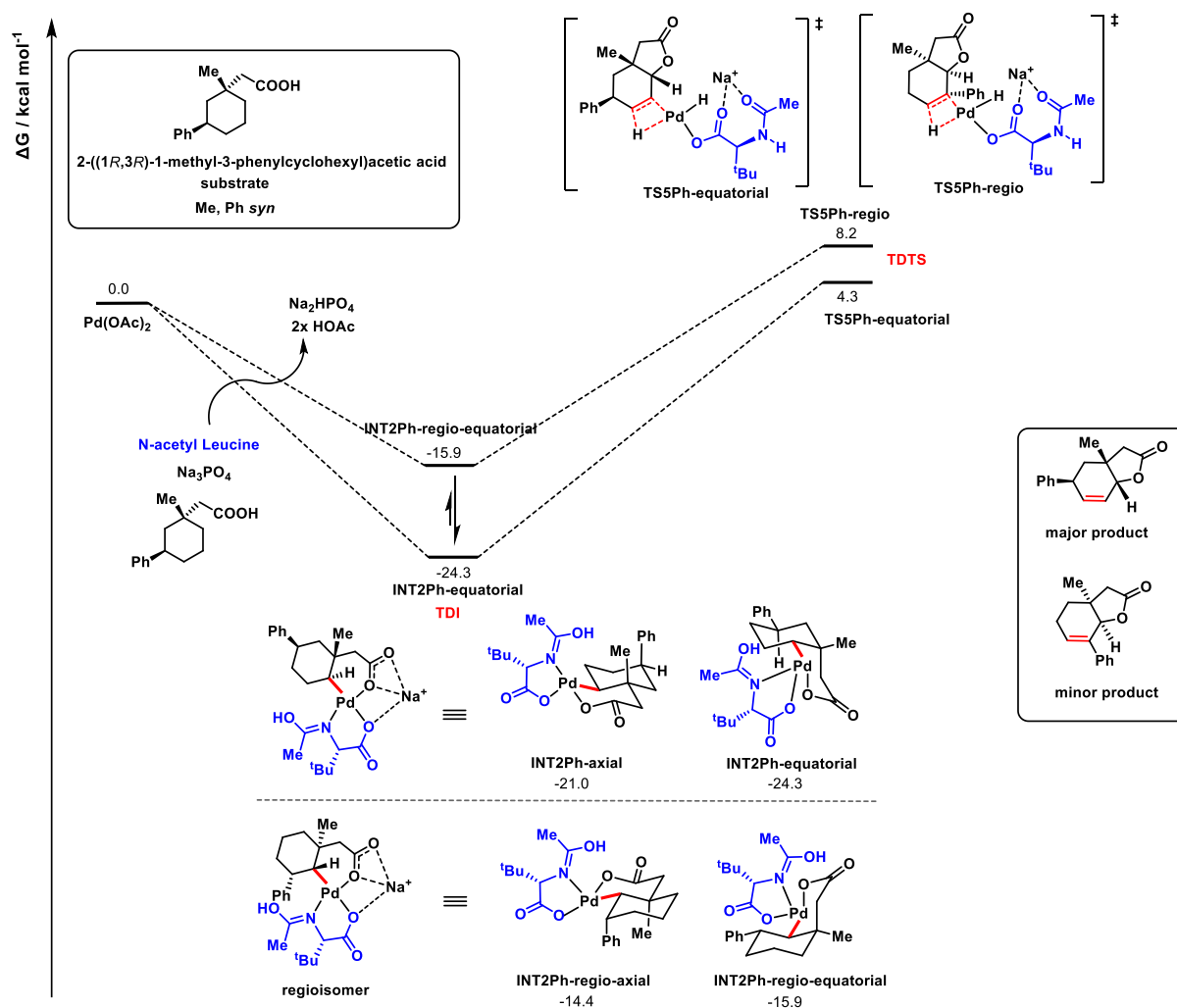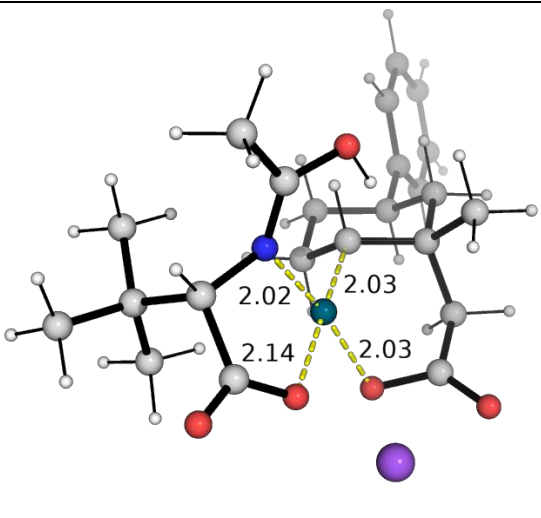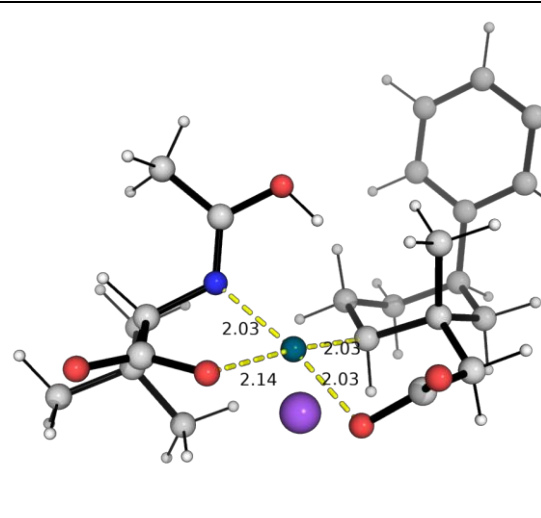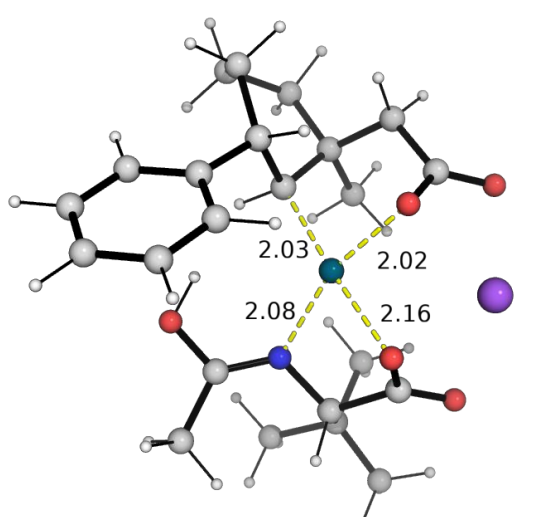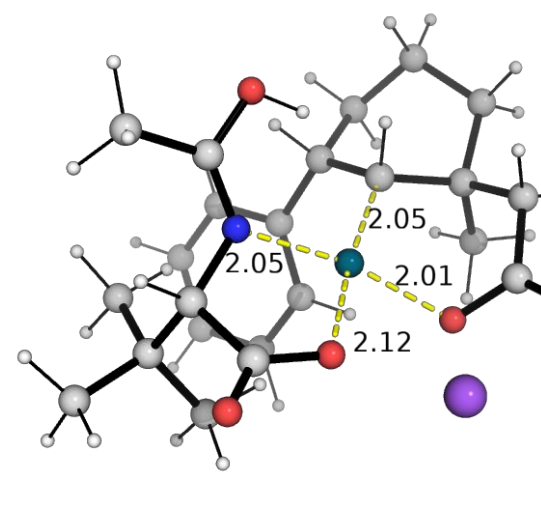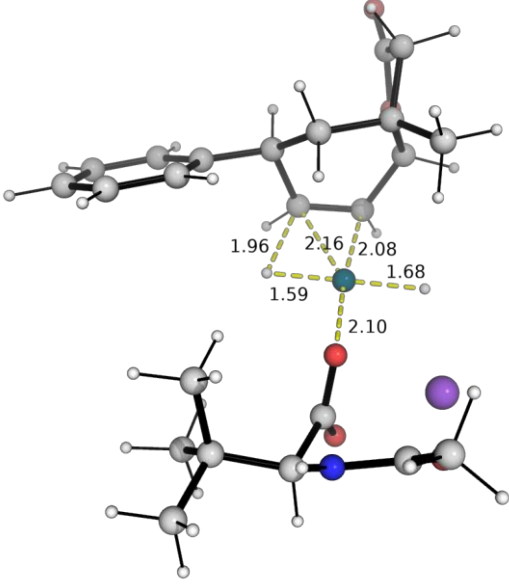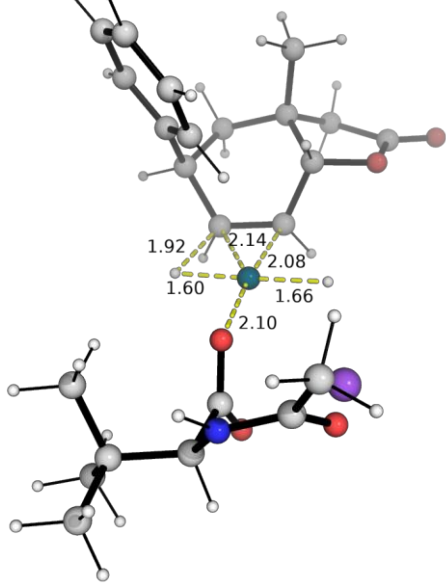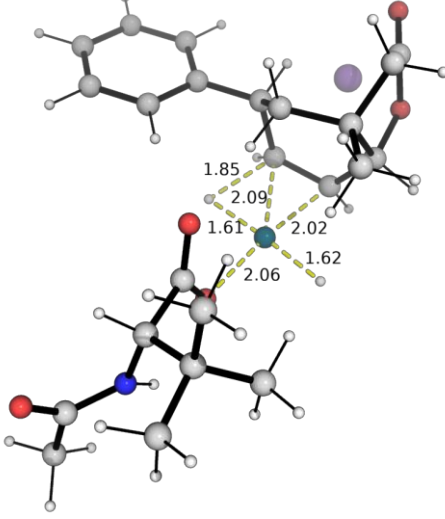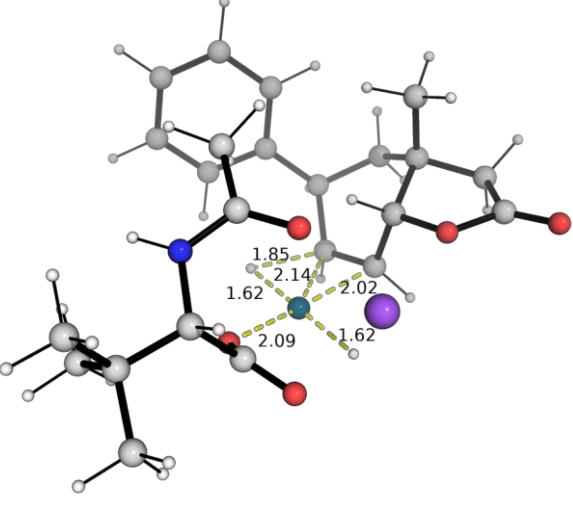
Figure S13. Gibbs energy profile for the turnover-frequency determining intermediate (TDI) and transition state (TDTS) for the functionalisation of 3-substituted substrate.

INT2Ph-equatorial	INT2Ph-axial
ΔG = -24.3 kcal mol⁻¹	-21.0 kcal mol⁻¹
INT2Ph-regio-equatorial	**INT2Ph-regio-axial**
ΔG = -15.9 kcal mol⁻¹	-14.4 kcal mol⁻¹
TS5Ph-equatorial	**TS5Ph-axial**
ΔG‡ = 4.3 kcal mol⁻¹	12.3 kcal mol⁻¹

TS5Ph-equatorial-c2	**TS5Ph-axial-c2**
$\Delta G^{\ddagger}$ = 25.9 kcal mol^{-1}	22.3 kcal mol^{-1}
TS5Ph-regio	
$\Delta G^{\ddagger}$ = 8.2 kcal mol^{-1}	
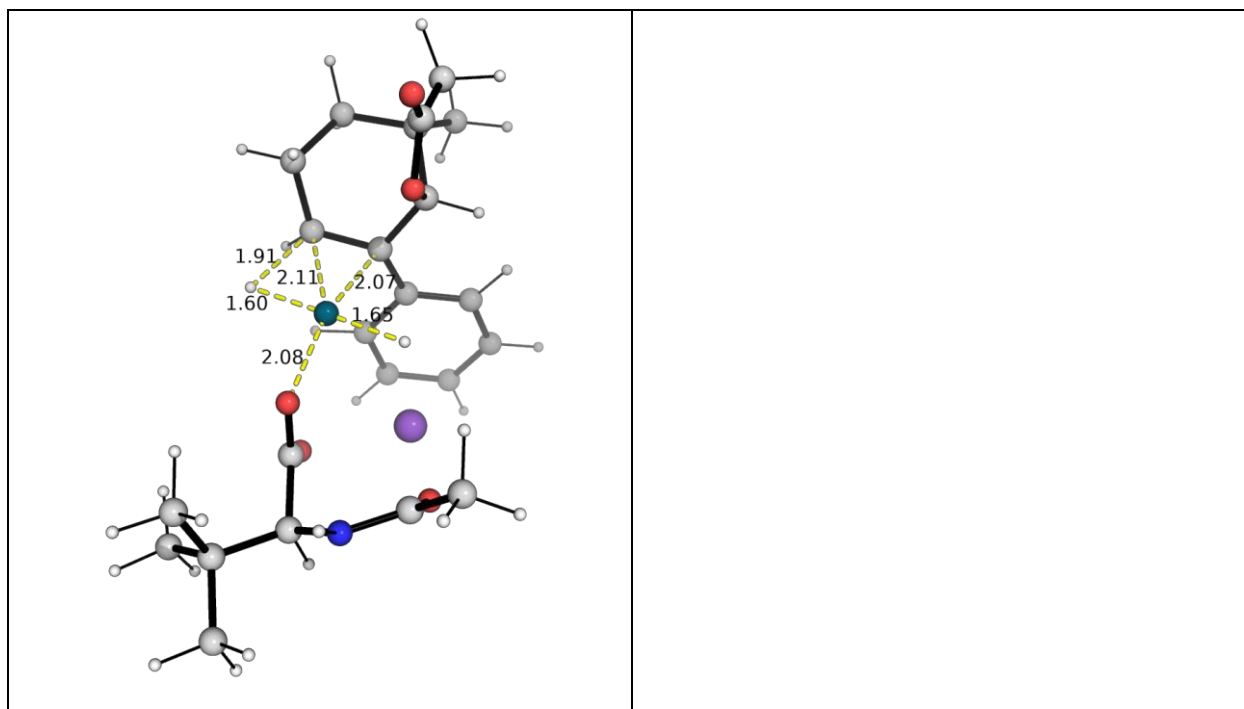
Figure S14. DFT optimised turnover frequency-determining intermediate (TDI) and transition state (TDTS) structures for the 3-substituted substrate. Gibbs energy values are taken relative to the sum of starting materials. Different transition state conformers are included and are denoted by c2, c3 etc, in increasing energy.

9.10. Optimized structures and absolute energies, zero-point energies

Geometries of all optimized structures (in *.xyz* format with their associated energy in Hartrees) are included in a separate folder named *final_xyz* with an associated readme.txt file. All these data have been deposited and uploaded to zenodo.org (https://zenodo.org/record/7516355; DOI: 10.5281/zenodo.7516355).

Absolute values (in Hartrees) for SCF energy, zero-point vibrational energy (ZPE), enthalpy and quasi-harmonic Gibbs free energy (at 120ºC/393.15 K) for optimized structures are given below. Single point corrections in SMD hexafluoroisopropanol using MN15/def2-QZVP level of theory are also included.

Structure	E/au	ZPE/au	H/au	T.S/au	qh-G/au	SP SMD MN15/def2-QZVP
HOAc	-228.644533	0.062197	-228.574711	0.041723	-228.61541	-229.06457600

acetate	-228.059294	0.048219	-228.00312	0.04228	-228.044179	-228.592055
PdOAc2_monomer	-583.809931	0.104326	-583.68809	0.068364	-583.753096	-584.634037
Na_substrate_2_salt	-663.638026	0.230412	-663.38552	0.076065	-663.458441	-664.677056
substrate_2	-502.040305	0.241876	-501.77836	0.069148	-501.845831	-502.967425
Na2HPO4	-966.579407	0.029498	-966.53614	0.057707	-966.592495	-967.610931
Na3PO4	-1128.161176	0.019146	-1128.1266	0.061821	-1128.187368	-1129.292047
Nacetyltertleucine	-593.162022	0.230084	-592.90756	0.080011	-592.984379	-594.257468
hfip	-788.500116	0.064458	-788.42028	0.061798	-788.480223	-789.866397
Ag2CO3	-556.727692	0.017256	-556.6994	0.055206	-556.753788	-557.239514
Pd_leucine_2hfip	-2296.722852	0.341101	-2296.3255	0.155423	-2296.46888	-2300.5114
lactone_prd	-499.613569	0.196067	-499.40007	0.062779	-499.461986	-500.529069
lactone_prd-c2	-499.620948	0.196417	-499.40723	0.062024	-499.468845	-500.536485
INT1'	-1383.335648	0.43882	-1382.8495	0.129897	-1382.972713	-1385.432754

TS1'	-1383.323155	0.43538	-1382.8415	0.126011	-1382.962016	-1385.413749
INT2'	-1383.364381	0.441078	-1382.8764	0.127674	-1382.998363	-1385.456831
INT1'-c2	-1383.342748	0.439502	-1382.856	0.131174	-1382.979685	-1385.440655
TS1'-c2	-1383.320921	0.436012	-1382.839	0.125391	-1382.958815	-1385.411889
INT2'-c2	-1383.354526	0.441179	-1382.8665	0.126831	-1382.988131	-1385.447502
INT1''	-1383.343151	0.439278	-1382.8567	0.13052	-1382.979811	-1385.441807
TS1''-c2	-1383.329042	0.435238	-1382.8477	0.127481	-1382.968455	-1385.420691
INT2''	-1383.365984	0.440823	-1382.8783	0.129708	-1383.000675	-1385.459128
TS2''	-1383.279908	0.438468	-1382.7939	0.136725	-1382.919805	-1385.381637
TS2''-c2	-1383.264164	0.43842	-1382.7786	0.132998	-1382.902705	-1385.370122
INT1''-c2	-1383.342957	0.439803	-1382.8562	0.130316	-1382.978913	-1385.440542
TS1''	-1383.333053	0.43579	-1382.8514	0.126471	-1382.971542	-1385.425058
INT2''-c2	-1383.361396	0.44101	-1382.8736	0.129636	-1382.995893	-1385.455347

INT1	-1383.343325	0.439916	-1382.8563	0.129438	-1382.979185	-1385.440646
TS1	-1383.327851	0.435623	-1382.846	0.126501	-1382.966669	-1385.41921
TS1-c2	-1383.322726	0.436062	-1382.8408	0.125248	-1382.960493	-1385.414883
INT2	-1383.366115	0.441226	-1382.8782	0.126819	-1382.999607	-1385.4595
INT2-c2	-1383.366115	0.441228	-1382.8782	0.126815	-1382.999606	-1385.459521
INT3a	-1383.320589	0.438974	-1382.8341	0.130558	-1382.957934	-1385.431006
INT3	-1383.344464	0.43888	-1382.8569	0.139031	-1382.985178	-1385.446155
TS2	-1383.338477	0.437974	-1382.853	0.135594	-1382.97858	-1385.439945
INT4	-1383.340493	0.437925	-1382.8539	0.138773	-1382.982176	-1385.441536
TS3	-1383.332195	0.43513	-1382.849	0.136164	-1382.975425	-1385.433272
INT5	-1383.338328	0.436855	-1382.8529	0.137179	-1382.980274	-1385.439261
INT5-c2	-1383.336579	0.437138	-1382.851	0.136232	-1382.977823	-1385.437325
INT6	-1383.30662	0.436092	-1382.8216	0.140235	-1382.950205	-1385.42623

TS4	-1383.282682	0.435416	-1382.7995	0.136458	-1382.925685	-1385.40426
TS4-c2	-1383.278811	0.434536	-1382.796	0.136282	-1382.922753	-1385.381705
TS4'	-1383.288948	0.435196	-1382.8054	0.138342	-1382.932889	-1385.389267
INT7	-1383.249681	0.436333	-1382.7656	0.134317	-1382.890737	-1385.411514
INT7-c2	-1383.286997	0.436392	-1382.8027	0.136092	-1382.92865	-1385.409455
TS5	-1383.290487	0.432471	-1382.8106	0.13477	-1382.935867	-1385.396015
TS5-c2	-1383.290714	0.432382	-1382.8113	0.129501	-1382.93409	-1385.389864
TS5-c3	-1383.231182	0.431733	-1382.7522	0.1333	-1382.876281	-1385.372786
TS5-c4	-1383.248007	0.431787	-1382.7689	0.1314	-1382.892672	-1385.348645
INT8	-1383.337455	0.437343	-1382.8523	0.133859	-1382.977575	-1385.432126
INT8-c2	-1383.329525	0.436405	-1382.8447	0.134037	-1382.970905	-1385.426338
INT8-c3	-1383.315704	0.436002	-1382.8315	0.137518	-1382.95882	-1385.422172
INT9	-1383.290498	0.432857	-1382.8092	0.137526	-1382.936634	-1385.39617

INT9-c2	-1383.293609	0.433447	-1382.8125	0.131029	-1382.936539	-1385.393111
INT10	-1440.48886	0.25374	-1440.1936	0.123322	-1440.309722	-1442.151878
INT10'	-883.602395	0.23426	-883.33769	0.096314	-883.429468	-884.804197
INT11	-1439.307803	0.239055	-1439.0279	0.124309	-1439.143945	-1440.970405
INT11'	-1672.150065	0.300931	-1671.8028	0.13505	-1671.927464	-1674.704568
INT11'-c2	-1672.138611	0.30038	-1671.7916	0.134421	-1671.916467	-1674.687228
TS2''-ac	-1018.755777	0.270425	-1018.4539	0.100356	-1018.547966	-1020.185855
INT3''	-1383.349947	0.439982	-1382.8622	0.135325	-1382.987826	-1385.448716
TS2''	-1383.279908	0.438468	-1382.7939	0.136725	-1382.919805	-1385.381637
INT4''	-1383.325912	0.441611	-1382.8366	0.137826	-1382.963234	-1385.425169
TS3a	-1383.276909	0.438712	-1382.7903	0.137402	-1382.91709	-1385.379846
INT5a	-1383.2926	0.441924	-1382.8026	0.139008	-1382.93027	-1385.433396
TS3b	-1383.262465	0.438685	-1382.7766	0.131414	-1382.900103	-1385.370109

	-1383.316429	0.441099	-1382.8278	0.134185	-1382.953082	
INT5b						-1385.425482

9.11. References:

Full reference Gaussian 16:

Gaussian 16, Revision B.01, Frisch, M. J.; Trucks, G. W.; Schlegel, H. B.; Scuseria, G. E.; Robb, M. A.; Cheeseman, J. R.; Scalmani, G.; Barone, V.; Mennucci, B.; Petersson, G. A.; Nakatsuji, H.; Caricato, M.; Li, X.; Hratchian, H. P.; Izmaylov, A. F.; Bloino, J.; Zheng, G.; Sonnenberg, J. L.; Hada, M.; Ehara, M.; Toyota, K.; Fukuda, R.; Hasegawa, J.; Ishida, M.; Nakajima, T.; Honda, Y.; Kitao, O.; Nakai, H.; Vreven, T.; Montgomery Jr., J. A.; Peralta, J. E.; Ogliaro, F.; Bearpark, M.; Heyd, J. J.; Brothers, E.; Kudin, K. N.; Staroverov, V. N.; Kobayashi, R.; Normand, J.; Raghavachari, K.; Rendell, A.; Burant, J. C.; Iyengar, S. S.; Tomasi, J.; Cossi, M.; Rega, N.; Millam, J. M.; Klene, M.; Knox, J. E.; Cross, J. B.; Bakken, V.; Adamo, C.; Jaramillo, J.; Gomperts, R.; Stratmann, R. E.; Yazyev, O.; Austin, A. J.; Cammi, R.; Pomelli, C.; Ochterski, J. W.; Martin, R. L.; Morokuma, K.; Zakrzewski, V. G.; Voth, G. A.; Salvador, P.; Dannenberg, J. J.; Dapprich, S.; Daniels, A. D.; Farkas, Ö.; Foresman, J. B.; Ortiz, J. V; Cioslowski, J.; Fox, D. J. Gaussian, Inc., Wallingford CT, 2016.

(1)   Frisch, M. J. .; Trucks, G. W. .; Schlegel, H. B. .; Scuseria, G. E. .; Robb, M. A. .; Cheeseman, J. R. .; Scalmani, G. .; Barone, V. .; Petersson, G. A. .; Nakatsuji, H. .; et al. Gaussian 16, Revision B.01. 2016.

(2)   Yu, H. S.; He, X.; Li, S. L.; Truhlar, D. G. MN15: A Kohn–Sham Global-Hybrid Exchange–Correlation Density Functional with Broad Accuracy for Multi-Reference and Single-Reference Systems and Noncovalent Interactions. *Chem. Sci.* **2016**, *7* (8), 5032–5051.

(3)   Weigend, F.; Ahlrichs, R. Balanced Basis Sets of Split Valence, Triple Zeta Valence and Quadruple Zeta Valence Quality for H to Rn: Design and Assessment of Accuracy. *Phys. Chem. Chem. Phys.* **2005**, *7* (18), 3297–3305.

(4)   Weigend, F. Accurate Coulomb-Fitting Basis Sets for H to Rn. *Phys. Chem. Chem. Phys.* **2006**, *8* (9), 1057–1065.

(5)   Rappoport, D.; Furche, F. Property-Optimized Gaussian Basis Sets for Molecular

Response Calculations. *J. Chem. Phys.* **2010**, *133* (13), 134105.

(6) Andrae, D.; Häußermann, U.; Dolg, M.; Stoll, H.; Preuß, H. Energy-Adjustedab Initio Pseudopotentials for the Second and Third Row Transition Elements. *Theor. Chim. Acta* **1990**, *77* (2), 123–141.

(7) Fukui, K. Formulation of the Reaction Coordinate. *J. Phys. Chem.* **2005**, *74* (23), 4161–4163.

(8) Fukui, K. The Path of Chemical Reactions - The IRC Approach. *Acc. Chem. Res.* **1981**, *14* (12), 363–368.

(9) Marenich, A. V.; Cramer, C. J.; Truhlar, D. G. Universal Solvation Model Based on Solute Electron Density and on a Continuum Model of the Solvent Defined by the Bulk Dielectric Constant and Atomic Surface Tensions. *J. Phys. Chem. B* **2009**, *113* (18), 6378–6396.

(10) Eberson, L.; Hartshorn, M. P.; Persson, O.; Radner, F. Making Radical Cations Live Longer. *Chem. Commun.* **1996**, No. 18, 2105–2112.

(11) Gu, X.; Song, X.; Shao, C.; Zeng, P.; Lu, X.; Shen, X.; Yang, Q. Electrospinning of Poly(Butylene-Carbonate): Effect of Solvents on the Properties of the Nanofibers Film. *Int. J. Electrochem. Sci.* **2014**, *9* (12), 8045–8056.

(12) Carraro, M.; Gardan, M.; Sartorel, A.; Maccato, C.; Bonchio, M. Hydrogen Peroxide Activation by Fluorophilic Polyoxotungstates for Fast and Selective Oxygen Transfer Catalysis. *Dalt. Trans.* **2016**, *45* (37), 14544–14548.

(13) Sigma-Aldrich. 1,1,1,3,3,3-Hexafluoro-2-propanol https://www.sigmaaldrich.com/catalog/product/aldrich/105228 (accessed Jun 6, 2017).

(14) Abraham, M. H.; Andonian-Haftvan, J.; Whiting, G. S.; Leo, A.; Taft, R. S. Hydrogen Bonding. Part 34. The Factors That Influence the Solubility of Gases and Vapours in Water at 298 K, and a New Method for Its Determination. *J. Chem. Soc. Perkin Trans. 2* **1994**, No. 8, 1777–1791.

(15) Richmond, E.; Yi, J.; Vuković, V. D.; Sajadi, F.; Rowley, C. N.; Moran, J. Ring-Opening Hydroarylation of Monosubstituted Cyclopropanes Enabled by Hexafluoroisopropanol. *Chem. Sci.* **2018**, *9* (30), 6411–6416.

(16) Berkessel, A.; Adrio, J. A. Dramatic Acceleration of Olefin Epoxidation in Fluorinated

Alcohols: Activation of Hydrogen Peroxide by Multiple H-Bond Networks. *J. Am. Chem. Soc.* **2006**, *128* (41), 13412–13420.

(17)   Winget, P.; Dolney, D. M.; Giesen, D. J.; Cramer, C. J.; Truhlar, D. G. Minnesota solvent descriptor database https://comp.chem.umn.edu/solvation/mnsddb.pdf (accessed Mar 15, 2022).

(18)   Grimme, S. Supramolecular Binding Thermodynamics by Dispersion-Corrected Density Functional Theory. *Chem.: Eur. J.* **2012**, *18* (32), 9955–9964.

(19)   Funes-Ardoiz, I.; Paton, R. S. GoodVibes v1.0.1 http://doi.org/10.5281/zenodo.56091.

(20)   Schrödinger, L. *The PyMOL Molecular Graphics Development Component, Version 1.8*; 2015.

(21)   Chen, G.; Gong, W.; Zhuang, Z.; Andrä, M. S.; Chen, Y. Q.; Hong, X.; Yang, Y. F.; Liu, T.; Houk, K. N.; Yu, J. Q. Ligand-Accelerated Enantioselective Methylene C(Sp^3)-H Bond Activation. *Science* **2016**, *353* (6303), 1023–1027.

(22)   Dutta, U.; Modak, A.; Bhaskararao, B.; Bera, M.; Bag, S.; Mondal, A.; Lupton, D. W.; Sunoj, R. B.; Maiti, D. Catalytic Arene Meta-C–H Functionalization Exploiting a Quinoline-Based Template. *ACS Catal.* **2017**, *7* (5), 3162–3168.

(23)   Cheng, G. J.; Yang, Y. F.; Liu, P.; Chen, P.; Sun, T. Y.; Li, G.; Zhang, X.; Houk, K. N.; Yu, J. Q.; Wu, Y. D. Role of N-Acyl Amino Acid Ligands in Pd(II)-Catalyzed Remote C–H Activation of Tethered Arenes. *J. Am. Chem. Soc.* **2014**, *136* (3), 894–897.

(24)   Yang, Y. F.; Hong, X.; Yu, J. Q.; Houk, K. N. Experimental-Computational Synergy for Selective Pd(II)-Catalyzed C–H Activation of Aryl and Alkyl Groups. *Acc. Chem. Res.* **2017**, *50* (11), 2853–2860.

(25)   Achar, T. K. T. K.; Zhang, X.; Mondal, R.; Shanavas, M. S. S.; Maiti, S.; Maity, S.; Pal, N.; Paton, R. S. R. S.; Maiti, D. Palladium-Catalyzed Directed *Meta*-Selective C–H Allylation of Arenes: Unactivated Internal Olefins as Allyl Surrogates. *Angew. Chem. Int. Ed.* **2019**, *58* (30), 10353–10360.

(26)   Porey, S.; Zhang, X.; Bhowmick, S.; Kumar Singh, V.; Guin, S.; Paton, R. S. R. S.; Maiti, D. Alkyne Linchpin Strategy for Drug:Pharmacophore Conjugation: Experimental and Computational Realization of a *Meta*-Selective Inverse Sonogashira

Coupling. *J. Am. Chem. Soc.* **2020**, *142* (8), 3762–3774.

(27) Kozuch, S.; Shaik, S. How to Conceptualize Catalytic Cycles? The Energetic Span Model. *Acc. Chem. Res.* **2011**, *44* (2), 101–110.

10. Deuterium Exchange Experiment:

In an oven-dried screw capped reaction tube was charged with magnetic stir-bar, corresponding acid (0.1 mmol), Pd(OAc)$_2$ (10 mol%), *N*-Ac-*t*Leu (20 mol%), Ag$_2$CO$_3$ (2 equiv.), and Na$_3$PO$_4$ (2 equiv.) in 1 mL of deuterated version of 1,1,1,3,3,3-hexafluoro-2-propanol (d^2-HFIP) were added. The reaction tube was capped and placed in a preheated bath at 120 °C with stirring (800 rpm) for 24 h. Upon completion the mixture was diluted with EtOAc and filtered through a celite pad. The filtrate was evaporated under reduced pressure and NMR of the crude mixture was taken. γ-Methyl group was found to be 59% deuterated and γ-methylene 45% deuterated.
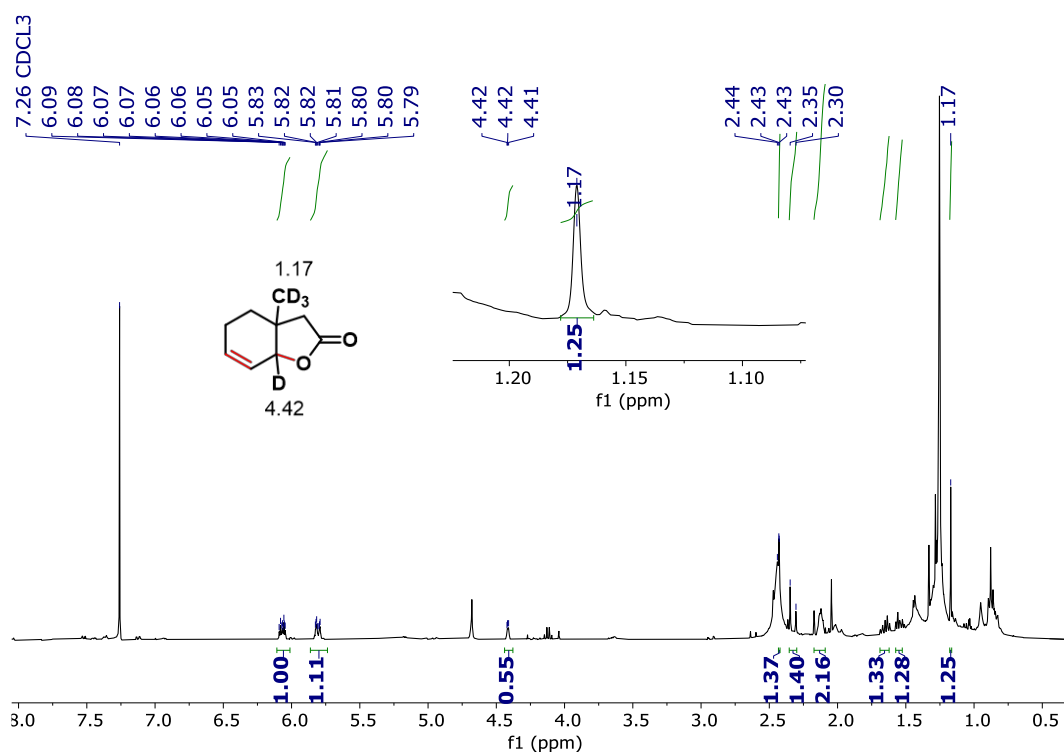

Figure S15. ^{1}H NMR spectra of product performed in d^2-HFIP.

Chemical competence of the alkenoic acid 5f.